JGR Solid Earth

RESEARCH ARTICLE
10.1029/2020JB019829

Key Points:
- Supershear ruptures within bimaterial interfaces possess unique characteristic properties
- Supershear properties depend on their propagation direction
- A number of these properties are explained by our accompanying analytic solution

Supporting Information:
- Supporting Information S1

Correspondence to:
J. Fineberg,
jay@mail.huji.ac.il

Citation:
Shlomai, H., Adda-Bedia, M., Arias, R. E., & Fineberg, J. (2020). Supershear frictional ruptures along bimaterial interfaces. *Journal of Geophysical Research: Solid Earth*, *125*, e2020JB019829. https://doi.org/10.1029/2020JB019829

Received 30 MAR 2020
Accepted 30 JUL 2020
Accepted article online 8 AUG 2020

Supershear Frictional Ruptures Along Bimaterial Interfaces

H. Shlomai[1], M. Adda-Bedia[2], R. E. Arias[3], and Jay Fineberg[1]

[1]The Racah Institute of Physics, The Hebrew University of Jerusalem, Jerusalem, Israel, [2]Université de Lyon, Ecole Normale Supérieure de Lyon, Université Claude Bernard, CNRS, Laboratoire de Physique, Lyon, France, [3]Departamento de Física, Facultad de Ciencias Físicas y Matemáticas, Universidad de Chile, Santiago, Chile

Abstract We experimentally and analytically explore supershear ruptures that are excited at the onset of frictional motion within "bimaterial interfaces," frictional interfaces formed by contacting bodies having different elastic (or geometric) properties. Our experiments on PMMA blocks sliding on polycarbonate show that the structure, transition sequence, and range of existence of such supershear ruptures are highly dependent on their propagation direction relative to the slip direction in the softer of the two materials. These properties are characterized for both the positive (parallel) and negative (antiparallel) propagation directions. An analytic, fracture-mechanics based description of supershear ruptures is derived. The theory quantitatively predicts both supershear structure and the allowed propagation range of supershear ruptures. The latter compares well with both the experimentally observed supershear ruptures in the negative direction as well as localized slip pulses in the positive direction, whose propagation speed lies between the shear velocities of both materials. Supershear ruptures in the positive direction, which are composed of trains of propagating slip pulses, evade this theoretical description.

1. Introduction

Frictional motion of contacting bodies will take place once the frictional resistance between the two bodies is overcome by applied external forces. The source of this resistance is due to the points of contact (asperities) across the interface that separates the contacting bodies. At the onset of frictional slip, not all of these contacts detach simultaneously. Indeed, the onset of slip is governed by propagating rupture fronts (Ben-David et al., 2010; Rosakis et al., 1999; Rubinstein et al., 2004; Shlomai & Fineberg, 2016) that break contacts at the front's leading edge. Local slip is only initiated in their wake. In the particular example of contacting tectonic plates, these propagating ruptures are also identified (Ben-Zion, 2001; Scholz, 2002) with the onset of earthquake dynamics.

This paper focuses on ruptures that propagate faster than shear wave speeds ("supershear") within frictional interfaces composed of elastically different materials (bimaterial interfaces). The work presented here is both experimental and theoretical. Supershear ruptures are important in that both their signatures and their increased potential to generate damage along natural faults are quite different than subshear ruptures. These ruptures have been fairly well studied in the context of "homogeneous interfaces" (where the frictional interface is bounded by *identical*materials), but relatively little experimental or theoretical work has been performed when their propagation takes place within bimaterial interfaces. As we will explain in this section, bimaterial interfaces are both very general and have rather unique characteristics. These interface properties will give rise to correspondingly unique rupture fronts, when bimaterial interfaces start to slip. The focus of the work presented here will be to provide an in-depth description of bimaterial supershear ruptures. While previous work has shown that such ruptures exist (Shlomai & Fineberg, 2016; Xia et al., 2005), mainly qualitative observations were provided. Here, through experiments, we will present, for the first time, the rather interesting properties and structures of this class of ruptures and demonstrate how these critically depend on their directionality. We will additionally describe how they transition from either rest or subsonic ruptures. Our accompanying theoretical analysis will provide the first explanation of how and why different modes of bimaterial ruptures are dynamically limited to narrow ranges of propagation velocities.

In the introductory section, we first present a rather comprehensive review of the work that has been performed both in bimaterial and homogeneous interfaces. We believe that such a broad introduction is

necessary in order to understand the general context of our results. We will then present new experimental results describing rupture characteristics in this important regime. This description will be followed by a new theoretical analysis for ruptures in this regime. Our theoretical results will then be compared to the experiments. In the final section, we discuss these results and their overall significance.

For clarity, we would like to define some of the terms in use within this paper, to avoid any ambiguity. When we refer to "stable" ruptures, we mean that such ruptures are mathematically stable; the ruptures are sustained (steadily propagating or even growing) but do not change their character. When a rupture mode becomes "unstable," we mean that the mode changes its character (or bifurcates). For example, a subsonic rupture could lose its stability (become unstable) and transition to either supershear ruptures or slip pulses. We define a "steady-state" rupture as one that propagates without changing either its mode of rupture or propagation velocity.

1.1. Ruptures Along Homogeneous Interfaces

When frictional interfaces separate identical materials (homogeneous interfaces), recent experiments have demonstrated (Bayart et al., 2016a, 2016b; Svetlizky & Fineberg, 2014; Svetlizky, Bayart, et al., 2017; Svetlizky, Kammer, et al., 2017; Svetlizky et al., 2016) that frictional rupture fronts propagating at velocities less than the Rayleigh wave speed, C_R, are identical to dynamic shear cracks—although, theoretically, the form of frictional ruptures could be influenced by friction laws (Barras et al., 2020). Shear cracks, which are quantitatively described in the framework of linear elastic fracture mechanics (LEFM) (Freund, 1990), have characteristic singular stresses at their tips having the universal form $\sigma_{ij} \propto K\,\Sigma_{ij}(C_f,\theta) / r^{1/2}$. Here, (r,θ) are polar coordinates with their origin at the crack tip, K is the dynamic stress intensity factor, and Σ_{ij} is a known function of the instantaneous front velocity C_f and the polar angle θ.

Shear fractures are also able to propagate above C_R. Within homogeneous media, ruptures propagating between the shear wave velocity, C_S, and the material dilatational velocity, C_P, are coined "supershear" ruptures. They had, for many years, existed only in theory (Albertini & Kammer, 2017; Andrews, 1976; Broberg, 1994, 1999; Dunham & Archuleta, 2004; Liu & Lapusta, 2008; Liu et al., 2014; Mello et al., 2010). This situation changed dramatically over the past two decades (Ben-David et al., 2010; Kammer et al., 2018; Mello et al., 2016; Rosakis et al., 1999, 2007; Rubinstein et al., 2004; Svetlizky et al., 2020), as supershear ruptures have been conclusively observed experimentally, once such measurements became technically possible. Supershear ruptures will occur when the elastic energy stored in the stressed material is sufficiently high, prior to the rupture onset (Ben-David et al., 2010; Kammer et al., 2018; Rosakis et al., 2007; Svetlizky et al., 2016; Wang et al., 1998; Xia et al., 2004). The transition to supershear ruptures can have extreme hysteresis, however (Kammer et al., 2018), so that they may be triggered by fault roughness or geometry (Barras et al., 2017; Bruhat et al., 2016; Dunham, 2007; Dunham et al., 2003; Liu & Lapusta, 2008) or even interactions with free surfaces (Hu et al., 2019; Kaneko & Lapusta, 2010). Supershear earthquakes along natural faults have also been, relatively recently, observed. Since the first such clear observations (Archuleta, 1984; Bouchon et al., 2001; Bouchon & Vallée, 2003), increasing numbers of possible supershear earthquakes have been revealed (Bao et al., 2019; Dunham & Archuleta, 2004; Wang et al., 2016).

1.2. Ruptures Along Bimaterial Interfaces

1.2.1. Symmetry Breaking and Bimaterial Coupling

Interfaces that separate materials that are not identical, either due to different elastic properties (Ampuero & Ben-Zion, 2008; Andrews & Ben-Zion, 1997; Weertman, 1980) or even geometrical shape (Aldam et al., 2016), are called *bimaterial* interfaces. Obviously, as most frictional interfaces in nature are bimaterial, frictional dynamics along such interfaces are the most general form of friction. Many natural faults are effectively bimaterial interfaces (Dor et al., 2008; Ma & Beroza, 2008; Langer et al., 2012; Lei & Zhao, 2009; McGuire & Ben-Zion, 2005). Bimaterial faults may be formed by contacting tectonic plates composed of different rock types. They may also be formed dynamically from initially homogeneous natural faults, after hundreds of years of accumulated slip or asymmetric damage zones on opposing sides of a fault (Dor et al., 2006).

Fundamental differences exist between ruptures along homogenous and bimaterial interfaces. The first clear difference is that, since bimaterial interfaces separate materials with different elastic properties, there are now two sets of shear waves and dilatational waves speeds in play. As a result, velocities and propagation regimes may exist in addition to the sub-Rayleigh and supershear velocity regimes of homogenous

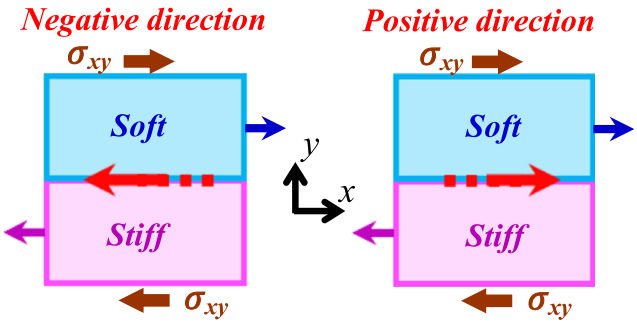

Figure 1. Rupture propagation directions. Ruptures propagating parallel to the slip direction of the softer material (right) are called ruptures in the "positive" direction. Rupture propagating in the opposite (antiparallel) direction (left) are defined as ruptures in the "negative" direction. Rupture directions are schematically denoted by red arrows, whereas slip directions in the soft material are denoted by blue arrows. In this paper, the positive direction will always be shown as propagating to the right.

systems. We define $C_S^{soft}(C_P^{soft})$ and $C_S^{stiff}(C_P^{stiff})$ as, respectively, the shear (dilatational) wave speeds of the softer and stiffer materials. Supershear ruptures are those which transcend $C_S^{stiff} > C_S^{soft}$. A velocity regime unique to bimaterial systems, called transonic velocities, occurs when rupture velocities are faster than C_S^{soft} but slower than C_S^{stiff}. Furthermore, analogs to Rayleigh waves (surface waves) along homogenous interfaces may or may not exist along bimaterial interfaces. These bimaterial surface waves are called generalized Rayleigh waves, C_{GR}, and their existence depends on the material contrast of the two media. In homogeneous media, C_{GR} become the familiar C_R as the material contrast goes to zero.

The loss of up-down symmetry in bimaterial interfaces, compared to homogeneous ones, produces major consequences. Dynamic shear ruptures always generate local slip along crack faces while propagating. Let us define $\vec{u}(x, y)$ as the displacement field within a 2-D material, where x is the direction along the propagation direction (along the interface) and y the direction normal to an interface located at $y = 0$. Across bimaterial interfaces, so long as no interface separation takes place, u_y is continuous across contacting faces, as are σ_{xy} and σ_{yy} as in homogeneous interfaces. In contrast to homogeneous interfaces, bimaterial interfaces, by definition, are not symmetric around $y = 0$. As a result, there is no a priori reason for the u_x displacements or slips, $\partial_t u_x$, to be symmetric across the interface. This asymmetry gives rise to a purely elastodynamic effect that relates the local slip velocity, $v_{slip} \equiv \partial_t u_x(x,0^+) - \partial_t u_x(x,0^-)$, at each point x along a bimaterial interface to normal stress variations, $\Delta\sigma_{yy}(x,0)$ at that point ($0^{\pm}$ refer to $y = 0$ coordinates when approaching the interface from below, $y = 0^-$, or above, $y = 0^+$) (Weertman, 1980). For a steady-state rupture front propagating at $C_f < C_S^{soft}$, this coupling has the form

$$\Delta\sigma_{yy}(x, y = 0) = \mu^*(C_f)\,\frac{v_{slip}}{C_f}, \tag{1}$$

where $\Delta\sigma_{yy}$ is the deviation of the normal stress from the applied normal stress (Ben-Zion, 2001). μ^* is a universal function of the rupture speed and the material contrast as well as other material parameters (Ranjith & Rice, 2001; Rice et al., 2001) and can be analytically calculated. μ^* may also depend on sample geometry (Aldam et al., 2016, 2017). The coupling in Equation 1 between the local slip and the local normal stress variations along bimaterial interfaces is called *bimaterial coupling*. The coupling coefficient, μ^*, generally increases significantly (Weertman, 1980) with C_f up to $\sim C_S^{soft}$.

The sign of the variation $\Delta\sigma_{yy}$ depends on the propagation direction of the rupture relative to the direction of the slip velocity induced by the rupture. When the slip direction in the soft material and propagation directions are parallel, as illustrated in Figure 1, the propagation direction is called "positive." When the slip direction in the soft material and propagation directions are antiparallel, the propagation direction is called the "negative" direction. In the positive direction, bimaterial coupling as predicted by Equation 1 (strongly decreased σ_{yy} and real contact area whose reduction depends strongly on local values of the slip velocities) has been verified experimentally (Shlomai & Fineberg, 2016) and numerically (Andrews & Ben-Zion, 1997; Ranjith & Rice, 2001). Moreover, when, experiments also showed that bimaterial coupling gives rise to "slip pulses," rupture fronts that are characterized by regions of strongly localized slip rate at their tips (Shlomai & Fineberg, 2016). We will differentiate between a "crack" and a "slip pulse" as follows. We define a crack as a rupture with a singular tip where the stresses, σ_{ij}, have the singular form $\sigma_{ij} \propto K \cdot r^{-1/2}$, where r is the distance from their tip. The slip along the interface, $\delta(x) \equiv u_x(x,0^+) - u_x(x,0^-)$, therefore, is spatially extended. A slip pulse is a rupture front where the majority of the slip occurs at very short distances from the rupture tip. Slip pulses do not possess the long power law ($r^{1/2}$) tails of the displacement field that characterize cracks. Slip pulse propagation velocities are thought to be limited by C_{GR} when it exists (Ben-Zion, 2001) and was numerically found to be either the slower shear wave speed (Rubin & Ampuero, 2007) or slightly higher than this value (Harris & Day, 1997; Scala et al., 2017), when C_{GR} does not exist.

More recent work (Shlomai et al., 2020) has looked more closely at how rupture fronts in the positive direction evolveinto slip pulses. This work found that, at $C_f < C_S^{soft}$, rupture fronts are well described by analytic solutions for bimaterial "cracks," which are analogous to the singular shear cracks observed within homogeneous interfaces. Slip pulses were only seen to exist at transonic velocities (experimentally, $C_S^{soft} < C_f < 1.04\, C_S^{soft}$). *New* analytic solutions for this regime were derived that described both the form of the leading edge of the measured slip pulses (described by $\sigma_{ij} \propto K \cdot r^{-q}$ where $0.1 < q < 1/2$) and the allowed maximal propagation velocity for slip pulses. Slip pulses are only formed for values of C_f at which σ_{yy} is reduced by the slip at the rupture tip; beyond the maximal velocity for slip pulses, σ_{yy} at all points along the interface will increase. Moreover, Shlomai et al. (2020) associated slip pulse localization with interface separation, which was numerically observed *only* when frictional coupling between σ_{yy} and σ_{xy} is enabled.

1.3. Predictions for Supershear Velocities

1.3.1. Theory

The main body of work on bimaterial supershear rupture velocities along bimaterial interfaces has been either theoretical or numerical. These calculations are highly sensitive to the boundary conditions chosen, and predictions can vary significantly. The main contributions to the current theoretical predictions of supershear propagation velocities and directions include the following:

- Exact analytical solutions for supershear ruptures propagating along the positive direction with a contact zone of size l behind the rupture tip (Wang et al., 1998). These calculations concluded that for any finite value of constant friction, only ruptures with velocities of up to $\sim \sqrt{2} C_S^{soft}$ can exist.
- Analytic stability analyses of the bimaterial coupling (Cochard & Rice, 2000; Ranjith & Rice, 2001) predicts that stable frictional supershear ruptures can propagate only in the negative direction, at velocities close to C_P^{soft}.
- Numerical observations of supershear velocities along bimaterial interfaces are highly correlated with the imposed velocity propagation during the nucleation process. Depending on the nucleation process and the prescribed friction law (Shi & Ben-Zion, 2006), supershear ruptures at velocities close to C_P^{soft} have been observed in the negative direction. Additionally, very rapid supershear ruptures have been observed in the positive direction (Shi & Ben-Zion, 2006) at velocities that approach the fastest sound wave velocity C_P^{stiff}.

The variety of the supershear velocity predictions emphasize the importance of obtaining experimental observations. These, however, have been quite sparse.

1.3.2. Experimental Observation of Supershear Velocities Along Bimaterial Interfaces

Only a few experiments have observed supershear ruptures along bimaterial interfaces. The observations of bimaterial supershear ruptures include the following:

- In a PMMA-steel system (Lambros & Rosakis, 1995b), triggering of supershear ruptures was achieved by impact. The material contrast in these experiments was very high, and all of the observed cracks were driven by the metal side, when the rupture tip was also loaded by waves reflected by the steel specimen. In this series of experiments, propagation velocities reached $1.5 C_S^{PMMA}$. These experiments were followed up by analytical solutions of elastic-rigid interfaces (Lambros & Rosakis, 1995a, 1995b; Liu et al., 1995). In experiments (Xia et al., 2005) with a smaller material contrast (formed by a polycarbonate-homalite-100 interface), ruptures were triggered by an exploding wire situated within the interface. Here, supershear ruptures were observed only along the negative direction at velocities close to the slower P wave velocity.
- Experiments (Shlomai & Fineberg, 2016) were also conducted where the nucleation of the supershear ruptures was quasi-static. In these experiments, conducted on a PMMA/polycarbonate system, a large amount of elastic energy was stored prior to the spontaneous nucleation of supershear ruptures. These experiments were the first to observe supershear ruptures in both the positive and negative directions with very different velocity distributions in each direction. The Shlomai and Fineberg (2016) experiments also studied the relative propensity of supershear ruptures. In the positive direction, the majority of ruptures were slip pulses with supershear ruptures very rarely observed. In the negative direction, slip pulses were not observed, and supershear ruptures were generally faster than those in the positive direction. These propagated at velocities that were concentrated around $0.85 C_P^{stiff}$.

1.4. The Transition to Supershear

Much research into supershear ruptures has focused on how subshear velocities can transition to supershear velocities by surpassing asymptotic velocities, such as the Rayleigh wave velocity for homogenous systems, or the limiting velocity for slip pulses (Shlomai et al., 2020). For homogeneous systems, the energy flowing into the rupture tip is both conserved and positive up to C_R. Beyond this asymptotic speed, the energy flux becomes *negative* (Freund, 1990) until the rupture becomes supershear. As a result, ruptures are not expected to smoothly accelerate from nucleation to supershear velocities through this energetically "forbidden" range of velocities. For bimaterial rupture, much effort has been devoted to determine an equivalent subshear limiting velocity (Cochard & Rice, 2000; Ranjith & Rice, 2001; Weertman, 1980). An energetic argument, however, that is in the same vein as for homogeneous systems remains elusive.

The most familiar mechanism that enables the transition to supershear velocities is via the well-known Burridge-Andrewstransition mechanism (Andrews, 1976; Burridge, 1973). This mechanism suggests that, ahead of a propagating rupture tip, at sub-Rayleigh (for homogenous) or subshear (for bimaterial) velocities, a secondary rupture can be nucleated by high-amplitude shear stresses imposed by shear waves that are radiated by the primary propagating rupture ahead of the rupture tip. Direct evidence of this mechanism has been experimentallyobserved within homogenous interfaces by spontaneously nucleated ruptures (Svetlizky et al., 2016).

In bimaterial systems, the transition to supershear has only been investigated by means of numerical simulations (Langer et al., 2012), wherethe transition mechanisms from subshear to supershear ruptures (Langer et al., 2012) in both propagation directions were compared. This work focused on the structure of the stress fields around the rupture tips in both directions and studied how variations of the normal stress at the interface impact both the ability to excite supershear rupture and the excitation mode in each direction. In the negative direction, while the normal stress increases behind the subshear rupture tip, it is reduced ahead of it. As a result, the interface is weakened in this region, making it easier for radiated shear stress waves to trigger a secondary supershearrupture ahead of the rupture tip. In bimaterials, this transition mechanism, while analogous to the Burridge-Andrews transition mechanism (Langer et al., 2012), is facilitated by the elastodynamically weakened interface ahead of the initial rupture tip. The transition gap to the supershear rupture, defined as the length of the segment between the subshear rupture and the supershear rupture, decreases with increasing material contrast. For a limited range of initial shear stresses, a smooth transition to supershear rupture was observed—as the transition length had shrunk beneath the numerical resolution. In this sense, these authors reported a smooth transition to supershear ruptures via the Burridge-Andrews transition mechanismin the negative direction.

In the work of Langer et al. (2012), a smooth transition was *not* observed along the positive direction. Here, as opposed to the negative direction, the transition gap was seen to increase with material contrast. The normal stress field structure was such that, in the positive direction, the normal stress increased ahead of the rupture tip and, thereby, increased the frictional resistance threshold. As a result, this mechanism suppressed any possible continuous transition to supershear ruptures of the primary propagating rupture tip in the positive direction.

2. Experimental System

2.1. Material Properties

Material shear, C_S, and longitudinal, C_P, wave speeds were obtained by measuring the time of flight of 5 MHz ultrasonic pulses. Due to the small wavelength (~0.5 mm) of the ultrasonic pulses used, compared to the dimensions of the measurement set-up of the sound wave velocities, the measured $C_P = C_{P,strain}$ corresponded to plane strain conditions ($\varepsilon_{zz} = 0$). The small z dimension (~5.5 mm) of the friction experimental set-up implies plane stress ($\sigma_{zz} = 0$) conditions in our experiments. Hence, throughout the analysis of the experiments, we will use $C_P = C_{P,stress}$ for plane stress conditions. The generalized Rayleigh wave speed, C_{GR}, does not exist for the material contrast of PMMA-PC system.

As both materials are viscoelastic, their elastic properties are effectively determined by the time scales that are relevant to the experiment (Read & Duncan, 1981). For our measurements, the material properties were determined by the 1–10 μs dynamic time scales in the vicinity of the propagating rupture tips. Thus, the wave

speeds in our experiments are determined by the "dynamic" elastic moduli that are observed at short time scales. The elastic properties and wave speeds of these materials are summarized in Table 1.

2.2. Loading Configuration

The experimental system used was that of Shlomai and Fineberg (2016) and presented schematically in Figure 2. In the experiments described here, the top block was clamped at its top face, while the bottom block was rigidly mounted at its bottom face within a stiff low-friction linear translational stage. The contacting faces of all blocks were diamond-machined to optical flatness. Both blocks were first compressed with a normal force F_N, which was varied between experiments throughout the range 2,000 N $< F_N <$ 6,000 N ($\sim$2 MPa $< \sigma_{yy} <$ 5 MPa). External shear loads, F_S, were then applied to the stiff translational stage, which was constrained in its movement only by the frictional resistance at the interface between the lower and upper blocks. In this way, F_S was spatially distributed along the entire length of the interface.

Both F_N and F_S were continuously monitored throughout the experiment by means of *S*-Beam load cells (of stiffness 10^6–10^7 N m^{-1}) in series with the loading apparatus. An optional rigid stopper of cross section 1 cm^2 could be applied to the top block at $x = 0$, at a controllable height h, to constrain motion of this edge in the x direction and control torquing. The application of the stopper thus introduced some elements of edge loading.

2.3. Loading Trigger Nucleation

To explore a range of external loading conditions, the experiments were conducted using two distinct ways to trigger rupture nucleation:

(1) F_S was applied to the system quasi-statically, at fixed F_N, at loading rates between 4 and 15 N s^{-1} until slip initiated. With this triggering method, ruptures generally nucleated within the quarter of the interface closest to $x = 0$, either as a result of the edge loading by the stopper or reduced local normal force resulting from induced torques.

(2) At the completion of a sequence of slip events, the residual F_S was kept fixed, and F_N was reduced at loading rates between 40 and 60 N s^{-1}, resulting in spontaneous rupture nucleation. This triggering method, via unloading, yielded a wider distribution of nucleation locations along the interface than in the former. In addition, these ruptures were generally more energetic than those that nucleated during the applications of shear. The reason for this is that high-shear strains were built up within the system, as a result of prior slip events, while the compressive loads were high, since the corresponding fracture energy ($\propto F_N$) was high (Bayart et al., 2018). When these trapped stresses were released upon unloading, normal loads (with correspondingly lower values of fracture energy) were much lower at rupture nucleation. As a result, ruptures nucleating via a reduction of normal load had much larger ratios of released strain energy to fracture energy.

For both nucleation (triggering) methods, ruptures could simultaneously nucleate in both directions. While rupture events occurred while either F_S or F_N were modified, the changes in F_S or F_N were sufficiently slow so that their values were effectively constant during the 0.1–0.2 ms rupture propagation period.

2.4. Real Contact Area Measurements

Changes in the real contact area along the entire interface were measured by means of an optical method based on total internal reflection. Basic principles are presented in detail elsewhere (Rubinstein et al., 2006, 2009). A sheet of light created by a high-power LED (CBT-120), incident on the frictional interface at an angle well beyond the critical angle for total internal reflection, was reflected everywhere except at the contact points. This yielded an instantaneous transmitted light intensity that was roughly proportional to $\mathscr{A}(x, z, t)$ over the entire $(x \times z)$ 200 $\times$ 5.5 mm interface. The transmitted light was continuously imaged (at a spatial resolution of 1,280 $\times$ 8 pixels) at 580,000 frames per second using a high-speed camera, Phantom v711, at 12 bit accuracy. Data acquisition was continuous with the data temporarily stored in a circular buffer large enough to acquire 7–13 ms of data, both before and after each event.

The frictional interface used was quasi-1-D, as its width (z direction), 5.5 mm, was much smaller than the other dimensions of the block. The simultaneous measurements of $\mathscr{A}(x, t) = \langle \mathscr{A}(x, z, t) \rangle_Z$ along the entire 1-D interface were obtained by averaging of the acquired images over the 8 pixels in the z direction. The noise level, after integration, was $\leq$1% of the signal.

Table 1
Elastic Properties of PMMA and Polycarbonate

Material	*P* wave	*S* wave	Density ρ	Poisson ratio ν	Young's modulus E
PMMA	Plane strain[a]: $2{,}680 \pm 10$ m.s^{-1} Plane stress[b]: $2{,}345 \pm 10$ m.s^{-1}	$1{,}361 \pm 13$ m s^{-1}	$1{,}170 \pm 1\%$ kg m^{-3}	Dynamic[a]: $0.33 \pm 0.2\%$ Static: 0.33	Dynamic[b]: $5.75 \pm 2.6\%$ GPa Static[c]: $3.62 \pm 1\%$ GPa
PC	Plane strain[a]: $2{,}192 \pm 10$ m s^{-1} Plane stress[b]: $1{,}653 \pm 10$ m s^{-1}	908 ± 20 m s^{-1}	$1{,}200 \pm 1\%$ kg m^{-3}	Dynamic: 0.39 Static: 0.33	Dynamic: $2.76 \pm 3.3\%$ GPa Static[d]: 2.4 GPa

[a]Directly measured by ultrasound. [b]Calculated directly from the measured values. [c]Measured by static measurements. [d]From literature.

2.5. Rupture Front Velocity C_f Calculation

We define the rupture front locations, x_{tip}, as the points where $\mathcal{A}(x_{tip}) = 0.95\mathcal{A}_0(x)$, where $\mathcal{A}_0(x)$ is the contact area measured immediately prior to rupture nucleation. Steadily propagating ruptures with propagation velocity C_f are defined as ruptures having no clear tendency to accelerate or decelerate over at least a region of 50 mm. $C_f(t)$ were obtained from differentiating $x_{tip}(t)$. Our precision in $C_f(t)$, which was determined by our 200 μm uncertainty in x, was less than 1%.

3. Experimental Results

We will now focus on experimental observations of supershear ruptures. When sufficient elastic energy is stored within the system prior to nucleation, supershear ruptures will be excited (Ben-David et al., 2010). If nucleation takes place within the central portion of the interface, we will observe simultaneous rupture propagation in both the positive and negative directions in both bimaterial and homogeneous interfaces. In Figure 3, we present a typical such experiment, where supershear ruptures develop in both directions.

While supershear ruptures along bimaterial interfaces can be excited in both the positive and negative propagation directions, in each direction, these ruptures are quite different from one another. These differences are evident in both how the system transitions to a supershear state and in the structure of supershear ruptures in each direction. In the following section, we will separately describe both the transition sequence and structure of each of these types of supershear ruptures.

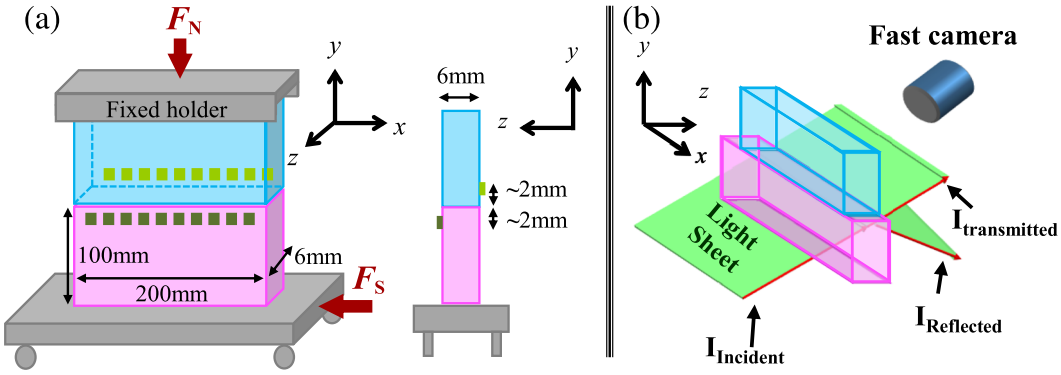

Figure 2. Experimental set-up. (a) Twenty rosette strain gauges (green squares) are mounted at heights ~2 mm above and beneath the interfaces at 10 locations along the frictional interface (left), on opposing block faces (center). F_N and F_S are the external normal and shear loads, respectively, that were applied to the system via load cells at the points indicated by red arrows. Each individual strain gauge (60 in number) was digitized at 1 million samples per second so that at each 1 μs throughout each experiment, we recorded the entire 2-D strain tensor, $\varepsilon_{ij}(t)$, at all 20 locations. (b) The instantaneous real contact area was measured along the entire contacting interface by a method based on total internal reflection (Rubinstein et al., 2004, 2006). We illuminated the frictional interface with a sheet of light at an incident angle that was sufficiently large so that the light underwent total internal reflection everywhere except at contacting points. The resulting transmitted light was roughly proportional to the real area of contact, $\mathcal{A}(x, t)$.

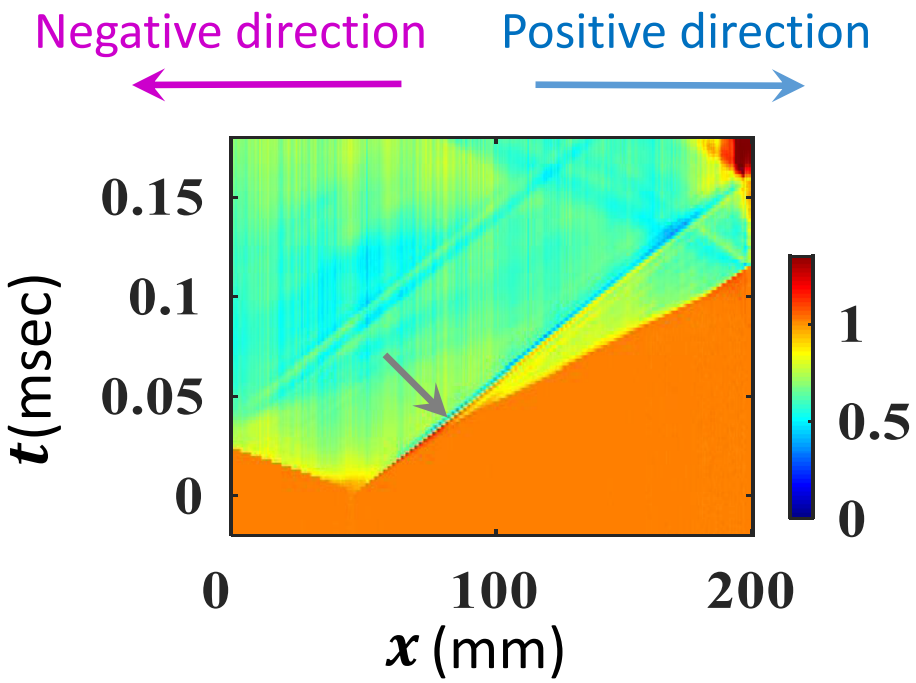

Figure 3. Energetic ruptures propagating in both propagation directions at velocities above C_P^{soft}. This rupture event nucleated at about one third of the interface and developed into two ruptures propagating in opposite directions away from the nucleation point. In the positive direction, the rupture first developed into a transonic slip pulse. Ahead of the transonic rupture tip, a secondary rupture nucleated (at approximately $x = 90$ mm denoted by the gray arrow) that propagated at the supershear velocity of $C_f^{positive} = 1,492\text{ms}^{-1} \sim 1.02C_P^{soft}$. In the negative (*left*) direction, the rupture immediately accelerated to a supershear velocity of $C_f^{negative} = 2,168\text{ms}^{-1} \sim 1.49C_P^{soft}$.

3.1. Supershear Ruptures in the Positive Direction

Supershear ruptures in the positive direction are, theoretically, predicted *not* to exist. This will be elaborated in section 4. Experimental observations show that supershear ruptures in the positive direction do exist but tend to be unstable. They do not nucleate directly and are only observed as secondary ruptures that nucleate ahead of steadily propagating slip pulses. Examples are presented both in Figure 4 and in the experiment presented in Figure 8. The slip pulses composing positive supershear ruptures are readily identified by characteristic reductions of the normal stress at their tip. This normal stress reduction results from bimaterial coupling (Shlomai & Fineberg, 2016; Shlomai et al., 2020) and is followed by rapid recovery of $\mathscr{A}(x,\ t)$ at slip pulse tails. This signature of slip pulses is reflected in the narrow dark blue region (of low $\mathscr{A}(x,\ t)$) at the tips of the slip pulses in Figures 3 and 4.

In the positive direction, supershear ruptures are experimentally observed to propagate at all velocities between C_S^{stiff} and C_P^{soft} (Shlomai & Fineberg, 2016), a subregime within the possible supershear velocity range. This observed velocity range is below numerical observations; supershear states have been numerically nucleated at velocities near $\sim C_P^{stiff}$ (Shi & Ben-Zion, 2006) and propagated at this velocity beyond the nucleation zone.

In Figure 4, we take a closer look at the transition from slip pulses to supershear ruptures. Figure 4a describes a typical event in which, eventually, a supershear rupture in the positive direction is formed. The transition to supershear is mediated by a train of successive slip pulses in the positive direction, each nucleated by a transient supershear rupture. The rupture originally initiated as a single transonic slip pulse that was triggered close to $x \sim 0$. As this rupture propagated, it generated radiation ahead of itself, as can be seen by the enhanced $\mathscr{A}(x,\ t)$ ahead of its tip in Figure 4b in the region $20\text{ mm} < x < 45\text{ mm}$. This radiated region expands with the slip pulse propagation distance, hence the radiation velocity is either supershear or rapidly transonic. The contact area increase within this radiated region indicates that the radiation contains an increased $\Delta\sigma_{yy}$ component.

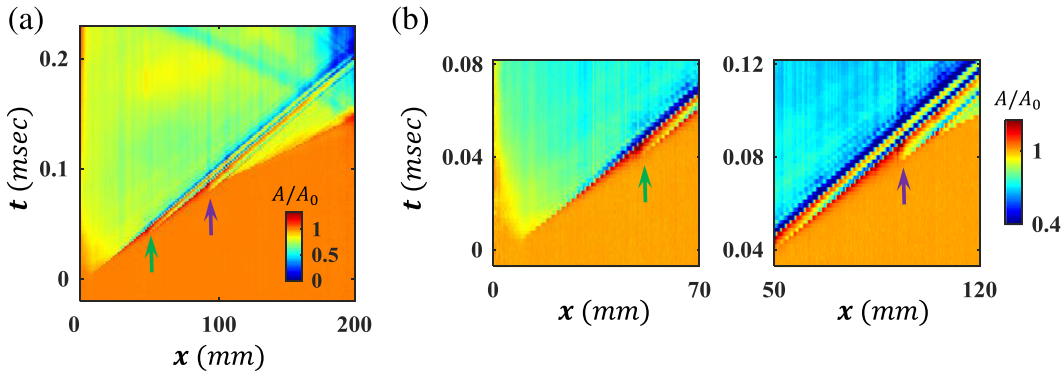

Figure 4. Positive supershear ruptures as slip pulse trains. (a) A slip pulse nucleates near $x = 0$ and propagates in the positive direction. Ahead of this rupture, a supershear rupture nucleates at $x \sim 55$ mm, as marked by the green arrow. Within a very short distance, the supershear rupture transitions to a second relatively strong slip pulse propagating ahead of the initial one and forming the basis for a "pulse train" (Shlomai & Fineberg, 2016). The radiation ahead of the second slip pulse nucleates a short-lived supershear rupture that nucleated a third slip pulse at $x \sim 95$ mm, denoted by the purple arrow. Its radiation triggered an additional supershear rupture at $x \sim 110$ mm, that itself continuously generated additional (weaker) slip pulses as it traversed the remainder of the interface. (b) Close-up of the slip pulses that form the pulse train in panel (a). The slip pulse fronts are followed by large releases of the contact area and are preceded by strong compressions with temporal and spatial widths of the same order of magnitude of the release width. The color coding of the close-up was adjusted to enhance the contact area variations.

The radiation ahead of the first slip pulse very quickly nucleates a *second* slip pulse that propagates *ahead* of the original one. The initial slip pulse continued to propagate (Shlomai et al., 2020) at $C_f \sim 1 - 1.04C_S^{soft}$ in the wake of the supershear rupture that preceded it, while further reducing the contact area. As Figure 4b demonstrates, the same process repeats ($50\text{ mm} < x < 90\text{ mm}$) itself; the second slip pulse radiates ahead of itself to form a third propagating slip pulse. In this way, supershear ruptures in the positive direction will typically generate new (relatively weak) slip pulses as they propagate. All of these slip pulses, themselves, continue to propagate at transonic velocities that are slightly above C_S^{soft}. They are therefore immediately outdistanced by the supershear rupture that nucleated them. This results in the "train" of parallel slip pulses evident in Figure 4. Once formed, these supershear fronts become the leading front that reduces most of the contact area.

At later times, the slip pulses generated by positive supershear ruptures are so dense that it is difficult to differentiate between them. These dense slip pulse trains are observed in both the contact area and the strain measurements, as apparent "noise" that follows the supershear front and precedes the main slip pulse. This "noise" in the strain measurements is strongly correlated to the weak slip pulses that are clearly revealed in the contact area measurements, as presented Figure 5.

Radiated shear waves, with a form similar to the radiated $\Delta\sigma_{yy}$ waves described above, would be expected in the Burridge-Andrews transition mechanism (Andrews, 1973; Burridge, 1973), which has been experimentally observed in homogenous systems (Svetlizky et al., 2016; Xia et al., 2004). In contrast to homogeneous systems, in bimaterial systems, the initial ruptures in the positive direction are not cracks but are always slip pulses. We believe that, in addition to an enhanced $\Delta\sigma_{yy}$ component, this radiation, which is evident in Figure 4, also contains enhanced shear stress components. While these are not directly observed here, enhanced radiated shear that accompanied radiated normal stress has been observed in simulations (Langer et al., 2012) that describe the bimaterial supershear transition in the positive direction. This mechanism appears to correspond to, essentially, the Burridge-Andrews mechanism for supershear generation.

It is of note that the slip pulses propagating in the wake of the supershear rupture tips are well separated from the radiation that generally occurs when slip pulses are initially formed. This radiation often masks the slip pulse structure. As a result, slip pulse trains formed during the supershear transition actually enable us to better observe the fine structure of steady-state slip pulses. It is now apparent that the steady-state structure of slip pulses includes a strong and rapid compression that immediately precedes the strong release of normal stress that characterizes slip pulses (Shlomai & Fineberg, 2016; Shlomai et al., 2020). This

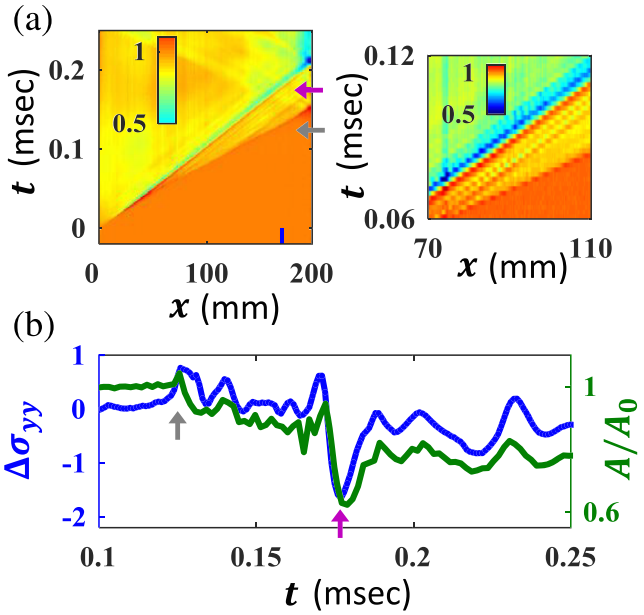

Figure 5. Positive supershear ruptures, composed of slip pulses, generate apparent noise. (a) The time-space evolution of the real contact area, $\mathcal{A}(x, t)$. Shown (left) is a slip pulse that nucleated near $x = 0$ and propagated in the positive direction. Here, a supershear rupture consequently nucleated and propagated ahead of the slip pulse. While propagating, it continuously triggered a dense train of weak slip pulses. These appear in the strain measurements as apparent "noise." (right) Close-up of the supershear front in which the numerous secondary slip pulses are shed by the supershear rupture are apparent. Adjustment of the color coding here was used to enhance observation of the weak slip pulses. (b) (blue line) The normal stress $\Delta\sigma_{yy}$ measured inside the stiff material at the location denoted in panel (a) by the vertical blue line. (green line) The contact area profile $\mathcal{A}(x_{sg}, t)$ at the measurement location of the $\Delta\sigma_{yy}$ signal. The passage of the supershear rupture is indicated by the gray arrow in both panels (a) (left) and (b). The large drop in both $\mathcal{A}(t)$ and $\Delta\sigma_{yy}^{stiff}$, indicated by purple arrows in both panels (a) (left) and (b), is due to the passage of initial strong slip pulse. The strong correlations in the large- and small-scale structures in both signals are strongly evident; the small amplitude fluctuating signals are generated by the passage of the weak slip pulses within the interval bracketed between the two arrows. This interval contains a dense train of weak slip pulses as seen clearly in panel (a) (right).

compression has a width that is approximately that of the normal stress drop (denoted by the arrow in Figure 5b). We believe that this localized compression is an essential part of the overall slip pulse structure.

3.2. Supershear Ruptures in the Negative Direction

We now consider bimaterial supershear propagation in the negative direction. The first distinction between supershear ruptures in the two propagation directions is a significant difference in their propagation velocities (Shlomai & Fineberg, 2016). This difference is clearly evident in Figure 6. The observed supershear velocity distribution in the negative direction (Figure 6, bottom) is entirely different than the distribution in the positive direction (Figure 6, top). Supershear velocities in the negative direction are all above C_P^{soft} and range to about 10–20% below C_P^{stiff}. The distribution of the negative supershear propagation velocities is also fairly bunched at 2,000 m s^{-1} $\sim 0.85C_P^{stiff} > C_P^{soft}$. This sharp empirical limit to the negative supershear velocities suggests that a theoretical limiting velocity may exist. Our measurements contrast with numerical calculations, where velocities of $\sim C_P^{soft}$ in the negative direction were observed (Ranjith & Rice, 2001; Shi & Ben-Zion, 2006).

The transition to supershear in the negative direction is also much different than in the positive one; the transition to negative supershear ruptures is always smooth. Figures 3 and 8 are typical examples where ruptures transition directly to supershear velocities in the negative direction. Such rapid transitions to supershear after nucleation are common. At times, the transition to supershear may occur more slowly, as presented in Figure 7. Here, the smooth nature of the transition to negative propagating supershear ruptures from a transient subshear rupture front is more readily apparent. There is no evidence of the indirect "Burridge-Andrews" type transition that characterizes the transitions in the positive direction (see, e.g., Figure 4).

Let us now consider the structure of negatively propagating supershear ruptures. The structures of counter-propagating supershear ruptures are compared in Figure 8. We find that the contact area (reflecting the normal stress) behind negative supershear rupture tips generally decreases by 50–60%, before rapidly recovering to levels of about 80% of the initial $\mathcal{A}(x, t)$ levels within a few mm. These strong $\mathcal{A}(x, t)$ variations are very similar to the strong localized variations of both $\mathcal{A}(x, t)$ and the normal stress behind the rupture tips of slip pulses propagating in the positive direction. While these $\mathcal{A}(x, t)$ variations are characteristic to negative supershear, they are significantly smaller than those within slip pulses. As a result, they are not always clearly observed. The similarity between the near-tip structure of positive transonic and negative supershear ruptures is consistent with the prediction that the sign of the bimaterial coupling in both cases is expected to be the same. In the same vein, as is clear from the example presented in Figure 8, analogous transient reductions of either $\mathcal{A}(x, t)$ or $\Delta\sigma_{yy}$ are *never* observed near the tips of supershear ruptures in the positive direction, where the sign of the bimaterial coupling is expected to *enhance* $\Delta\sigma_{yy}$ (as well as $\mathcal{A}(x, t)$) with increased slip velocities.

In the negative direction, supershear ruptures are dominant; roughly 61% of all experimentally observed negatively propagating ruptures (whose lengths were over 50 mm) were supershear. In contrast, in the positive direction supershear ruptures are relatively rare and constitute only 2% of observed ruptures (Shlomai & Fineberg, 2016). This relative stability of the negatively propagating supershear ruptures, together with the characteristic reduction of $\mathcal{A}(x, t)$ at their tips, is, again, wholly consistent with predicted bimaterial coupling; the reduction of $\Delta\sigma_{yy}$ in the negative direction should enhance negative supershear ruptures relative to negative subshear ruptures (which are suppressed by the bimaterial coupling induced *increase* of $\Delta\sigma_{yy}$).

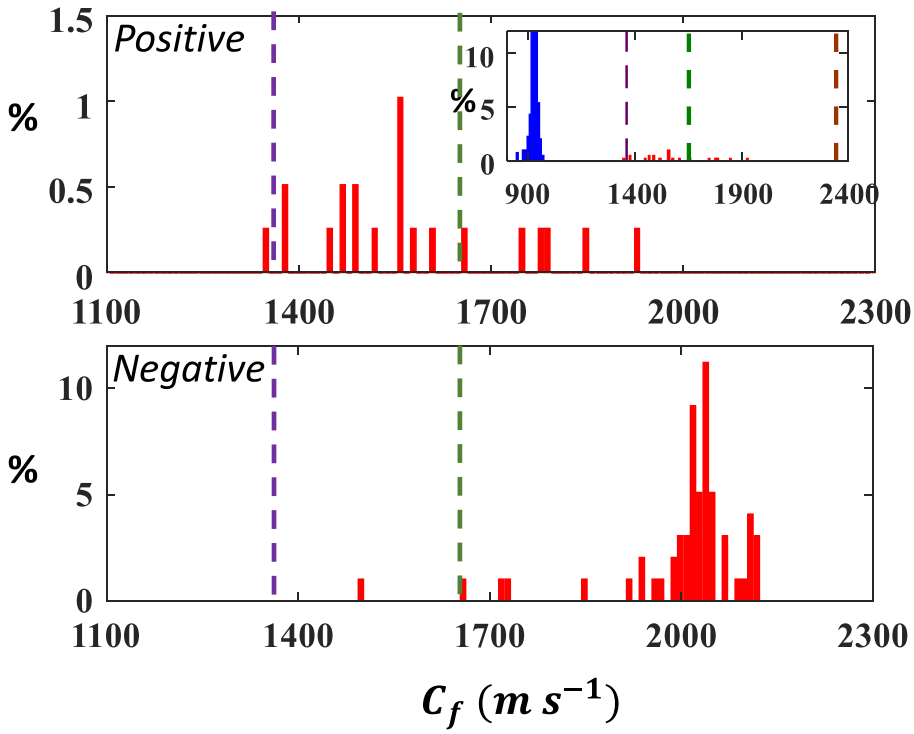

Figure 6. Supershear velocity distributions in both the positive and negative propagation directions. (top) The distributions of supershear front velocities. The distributions are presented as a percent of the *total* number of fronts that were observed to propagate in the positive direction. (inset) The distribution of *all* of the fronts in the positive direction. Transonic slip pulse distribution is in blue, whereas the supershear distribution (red) corresponds to the main panel. Note that the vast majority of fronts in the positive direction are slip pulses. (bottom) The distribution of observed supershear pulses in the negative direction. Normalization is as above (including subshear propagating fronts). In sharp contrast to the positive direction, the vast majority of fronts in the negative direction are *supershear*. C_S^{stiff}, C_P^{soft}, and C_P^{stiff} are denoted by, respectively, the purple, green, and brown dashed lines.

4. Theoretical Predictions for Supershear Ruptures

We now develop a new theoretical description for bimaterial supershear ruptures. This provides a framework in which we can better understand the experimental results described above. We consider the dynamic problem of a 2-D medium having a Mode II rupture propagating along a frictional interface on the plane $y = 0$ separating two linear isotropic elastic half spaces. The loading, slip motion, and rupture propagation are in the x direction, and all variables are functions of x, y, and t only. Shear and dilatational wave velocities are $C_S^n = \sqrt{\mu^n/\rho^n}$ and $C_P^n = \sqrt{(\lambda^n + 2\mu^n)/\rho^n}$, where ρ_n is mass density and λ_n and μ_n are Lamé coefficients. The subscript n refers to *soft* or *stiff* and denotes the top ($y > 0$) soft and bottom ($y < 0$) stiff materials, respectively. Here, as above, $C_S^{soft} < C_S^{stiff}$ and $C_P^{soft} < C_P^{stiff}$.

In contrast to Ranjith and Rice (2001), who analyzed the stability of perturbation along a fault that is already slipping, we consider here an in-plane rupture that propagates with a constant velocity C_f along the bimaterial interface. Thus, we consider a moving coordinate system $x = X - C_f t$. The bulk equations of motion are then given by

$$\frac{\partial \sigma_{ij}^{(n)}}{\partial x_j} = \rho_n C_f^2 \frac{\partial^2 u_i^{(n)}}{\partial x^2}, \tag{2}$$

where $x_1 \equiv x$ and $x_2 \equiv y$. In order to solve the rupture problem, we need to specify the boundary conditions along the interface. Motivated by experimental evidence of the persistence of crack face contact during the passage of the rupture front, we restrict our study to frictional contact in which both traction and normal

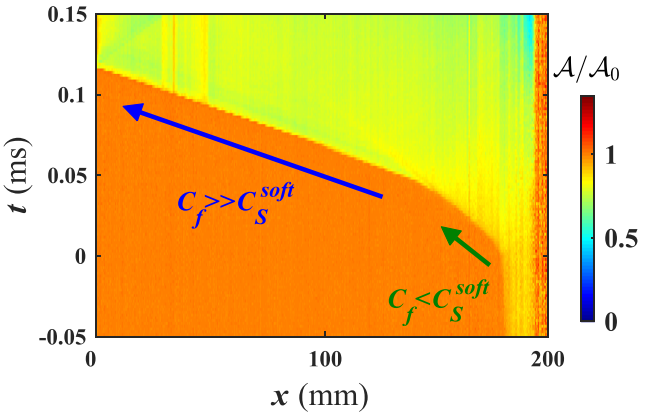

Figure 7. A slow and smooth transition to supershear in the negative direction. The rupture shown nucleated near $x = 200$ mm and propagated in the negative direction (left direction in this section). After nucleating, the rupture undergoes a short but distinct subshear stage at velocity $C_f = 830$ $ms^{-1} \sim 0.91 C_S^{soft}$, denoted by the green arrow. After ~25 mm of propagation, the rupture smoothly transitioned to a supershear rupture propagating at $C_f = 1,970 ms^{-1} \sim 0.9 C_P^{soft}$, as denoted by the blue arrow. After the transition, a faint decaying crack-like front can be observed within the wake of the supershear front.

displacement are continuous across the bimaterial interface. This frictional behavior is expressed through the following boundary conditions:

$$u_y^{(soft)}(x, 0^+) - u_y^{(stiff)}(x, 0^-) = 0, \tag{3}$$

$$\sigma_{yy}^{(soft)}(x, 0^+) - \sigma_{yy}^{(stiff)}(x, 0^-) = 0, \tag{4}$$

$$\sigma_{xy}^{(soft)}(x, 0^+) - \sigma_{xy}^{(stiff)}(x, 0^-) = 0. \tag{5}$$

In addition, the rupture tip separates two types of boundary conditions. Ahead of the tip ($x > 0$), we require the continuity of displacement (slip identically vanishes):

$$u_x^{(soft)}(x, 0^+) - u_x^{(stiff)}(x, 0^-) = 0; \qquad x > 0. \tag{6}$$

Behind the tip ($x < 0$), we specify the value of the shear stress at the boundary by the friction law along the interface. The physics of friction are embedded in this boundary condition behind the propagating front. Various boundary conditions are found in literature. Here, a simple crack-like boundary condition is assumed; one imposes that the shear stress behind the propagating tip drops to a constant residual value τ_R:

$$\sigma_{xy}(x, 0) = \tau_R; \qquad x < 0, \tag{7}$$

where the superscript is omitted when the normal and shear stress are evaluated along the interface. Note that, while bimaterial coupling may well create variations in σ_{yy}, our assumption of constant residual stress behind the crack's tip essentially negates any coupling between normal stress variations and the residual shear stress. We call this "frictionless" since τ_R can always be subtracted away, by superposition.

It was found (Shlomai et al., 2020) that the above formulation for transonic ruptures predicts crack-like ruptures whose functional form provides an excellent description of the form of the stress and strain fields in the vicinity of the rupture tips of experimentally observed subshear crack-like ruptures and transonic slip pulses.

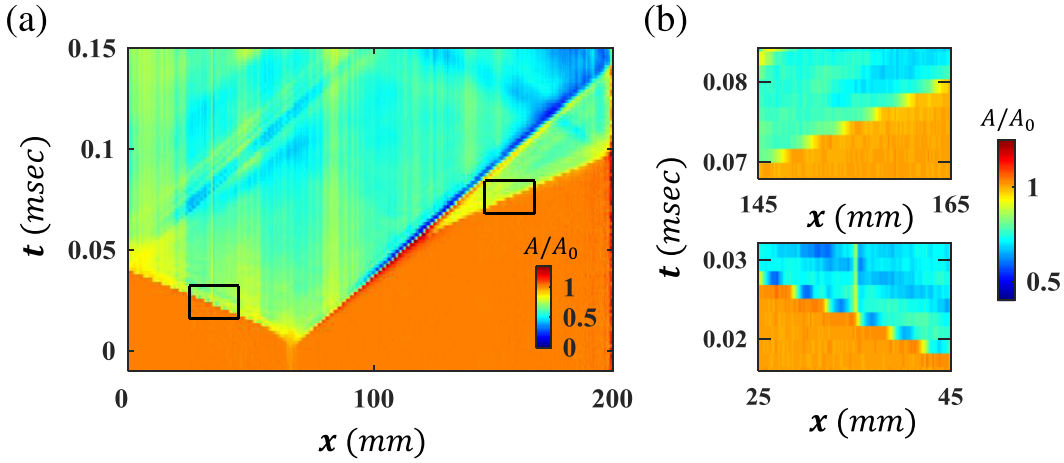

Figure 8. Comparison of the structures of supershear ruptures in both propagation directions. (a) In this event, ruptures nucleated at approximately $x = 80$ mm and propagated in both directions. Initially, the transition in the positive direction occurred via a transonic slip pulse with velocity $C_f^{positive} = 942$ $ms^{-1} \sim 1.04$ C_S^{soft} to a supershear rupture with $C_f^{positive} = 1925$ $ms^{-1} \sim 1.16 C_P^{soft}$. In the negative direction, the transition is smooth to a supershear rupture of velocity $C_f^{negative} = 1980 m.s^{-1} \sim 1.2 C_P^{soft}$. (b) Close-up of the contact area structure for the two supershear ruptures. (b, top) Positive supershear rupture. The contact area drops as a step function with the passage of the supershear rupture. The color coding of the insets was adjusted to enhance the contact area behavior. (b, bottom) Negative supershear rupture. The contact area initially drops to $\sim 0.6\mathcal{A}_0$, then first rapidly increases to $\sim 0.75\mathcal{A}_0$. $\mathcal{A}$ then subsequently decreases to its residual value. The initial rapid drop of the contact area closely resembles the release of the normal stress caused by the bimaterial coupling in the positive direction for transonic slip pulses. This can be seen as the characteristic dark blue line immediately behind slip pulse fronts propagating in the positive direction.

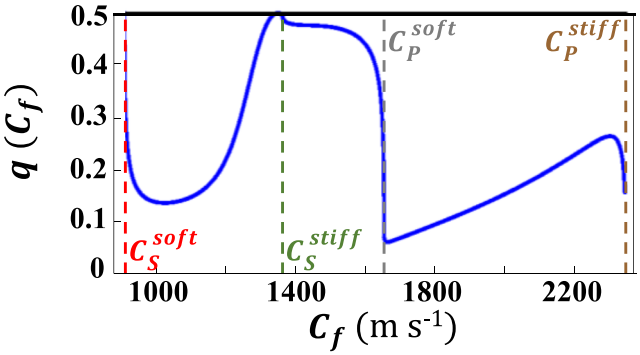

Figure 9. The exponent $q(C_f)$. Here, $q(C_f)$ is calculated using the material properties that correspond to the materials used in our experiments. Plane stress conditions are assumed. The dashed lines correspond to the wave speeds of the top and bottom samples. Notice that $q(C_f) = 1/2$ only for $C_f = C_S^{soft}$ and $C_f \approx C_S^{stiff}$.

In order to capture, however, the localization that characterizes slip pulses in this velocity regime, it was necessary to incorporate a nontrivial friction law (Amontons-Coulomb friction law) for $x < 0$.

The elastodynamic problem described above is well posed once both the applied loading at the remote boundaries and the motion of the rupture front are specified. In the following, we are interested in the behavior of the asymptotic stress field in the vicinity of propagating fronts whose speed is $C_S^{soft} < C_f < C_P^{stiff}$. Due to its wave character, the boundary value problem defined above should be solved separately for three different velocity regimes that depend on the strength of bimaterial contrast: $C_S^{soft} < C_f < C_S^{stiff}$, $C_S^{stiff} < C_f < C_P^{soft}$, and $C_P^{soft} < C_f < C_P^{stiff}$. In the supporting information, we provide a suitable approach for computing the asymptotic stress field in the vicinity of the propagating front and apply it to each velocity interval. The method of resolution is standard, and some computational steps are similar to previous studies on the subject; see, for instance, Wang et al. (1998). Nevertheless, this work gathers all of the cases in a single study. In the supporting information, we show that the general solution of the near-tip asymptotic stress field possesses a singularity which can be expressed at the interface $y = 0$ by

$$\sigma_{xy}(x, 0) = K_q \frac{H(x)}{x^{q(C_f)}}, \tag{8}$$

$$\Delta\sigma_{yy}(x, 0) = K_q \left(A^+(C_f) \frac{H(x)}{x^{q(C_f)}} + A^-(C_f) \frac{H(-x)}{(-x)^{q(C_f)}} \right), \tag{9}$$

where $H(\cdot)$ is the Heaviside function with coefficients A^+ and A^- describing the magnitude of the variations of $\Delta\sigma_{yy}$ ahead and behind the rupture tip, respectively. K_q is a stress intensity factor-like coefficient. Note that the sign of K_q is related to the propagation direction. The choice of the upper material to be the soft one imposes that if $K_q > 0$, the slip direction in the soft material (i.e., direction of applied shear) is in the positive direction and vice versa. In the supporting information, the exponent $q(C_f)$ is computed for any supershear speed and found to always satisfy $0 \le q(C_f) \le 1/2$ (see example in Figure 9).

While the elastic problem can be solved for any propagation speed, it does not constrain the resulting elastic fields to be physically consistent with rupture propagation. For an interface bounded by identical materials (a "homogeneous interface"), this is generally fulfilled for any propagation speed due to symmetry considerations. However, any bimaterial mismatch induces up-down symmetry breaking of the near-tip strain and stress fields across the interface, which could induce particle displacement that is inconsistent with the direction of the applied loading and/or rupture propagation. The computation of the velocity-dependent coefficients $A^{\pm}(C_f)$ is crucial for the determination of the allowed velocity regimes. The signs of $A^{\pm}(C_f)$, when coupled with the sign of K_q, determine the overall sign of $\Delta\sigma_{yy}$ in the vicinity of the rupture tip. We expect physically viable solutions only if the two $A^{\pm}(C_f)$ have different signs. This stems from an expectation that a moment must be existent around the crack tip at $x = 0$ that results from slip for $x < 0$ coupled to $u_x(x > 0, y = 0) = 0$. If we further require that bimaterial coupling will *reduce* $\Delta\sigma_{yy}$ behind the rupture tip, then the sign of $A^-(C_f)$ must be positive for slip in the positive direction (where $K_q > 0$) and *negative* for slip in the *negative* direction (where $K_q < 0$).

As we demonstrate in Figure 10, the above conditions are only satisfied within three discrete ranges of C_f for the parameters used in our experiments. In the positive direction, we expect to have a dynamic reduction of $\Delta\sigma_{yy}$ only within the transonic regime (shaded blue in the figure), as described in detail in Shlomai et al. (2020). In the supershear velocity regime, only an increase of $\Delta\sigma_{yy}$ is expected in the positive direction. As a result, no supershear ruptures are expected in this direction. In the negative direction, $\Delta\sigma_{yy}$ is reduced within two discrete regimes. The first of these is a thin (transonic) region of C_f near C_S^{stiff}. The second is a wider and well-defined region between $1,700\text{ms}^{-1} < C_f < 1,930\text{ms}^{-1}$.

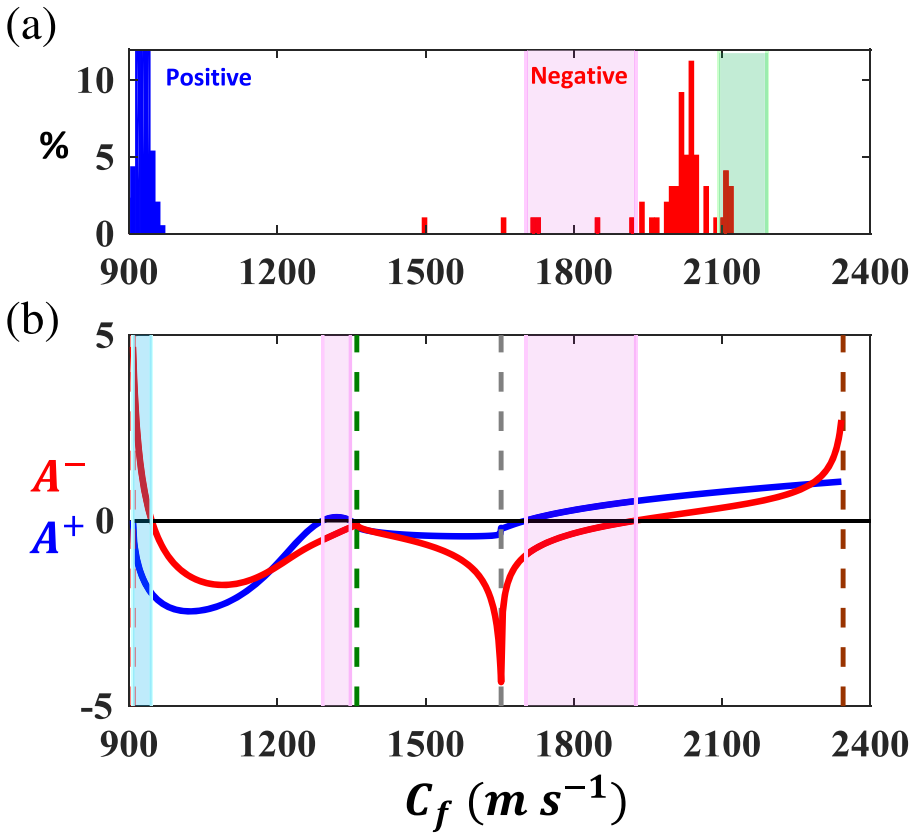

Figure 10. Comparison of the predicted and experimentally observed rupture propagation velocities. (a) Experimental rupture propagation velocity distributions of measured supershear rupture velocities in the negative direction (red) and of the transonic slip pulses in the positive direction (blue). The shaded pink (green) region corresponds to the faster branch of analytical solutions of rupture velocities when plane stress (plane strain) conditions are assumed. (b) The normal stress variations within the bimaterial interface. The coefficients A^+ and A^- describe the magnitude of the variations of σ_{yy} ahead and behind the rupture tip, respectively, for the bimaterial properties used in experiments. Plane stress conditions are assumed. Dashed lines correspond to the wave speeds of the top and bottom samples (from left to right: C_S^{soft} , C_S^{stiff}, C_P^{soft}, and C_P^{stiff}). Allowed supershear ruptures (see text) are those where A^+ and A^- have opposite signs. Furthermore, we require that $\Delta\sigma_{yy}$ be reduced behind the rupture tip; thus, the sign of $A^-(C_f)$ must be positive (negative) for slip in the positive (negative) direction. The shaded regions correspond to the allowed propagation velocities for the positive (blue) and negative (pink) directions. Note that in the positive direction, *only* transonic velocities are allowed (see text). The velocity regime corresponding to the (pink shaded) transonic branch with velocities close to C_S^{stiff} is not observed experimentally. This may be due to the fact that the magnitude of A^+ is very small, making it unlikely that a rupture front selects this velocity regime.

In Figure 10a, we present the observed range of supershear velocities in the negative direction for our experimental parameters and transonic velocities in the positive direction. We, indeed, find that the experimentally observed supershear ruptures occur in a region of velocities ($1,650\text{ms}^{-1}<C_f<2,050\text{ms}^{-1}$) that roughly corresponds to the finite range predicted by the theory for plane stress conditions (pink-shaded region). We note that the values of the wave speeds may shift slightly as a result of the finite width of our experimental samples. Recent studies of supershear ruptures within homogeneous interfaces (Svetlizky et al., 2020) have indeed demonstrated that effects due to finite sample thickness can increase longitudinal wave speeds by 3–4%. This shift toward higher velocities is consistent with the ~4% shift of the experimentally observed supershear velocities above predicted values.

In Figure 11, we present the complete theoretical phase diagram for bimaterial supershear ruptures in the negative direction. Presented are the allowed supershear velocities (scaled by C_S^{soft}) as a function of the material mismatch, $\gamma \equiv C_S^{soft}/C_S^{stiff}$ for model materials, whose parameters slightly differ from the experimental

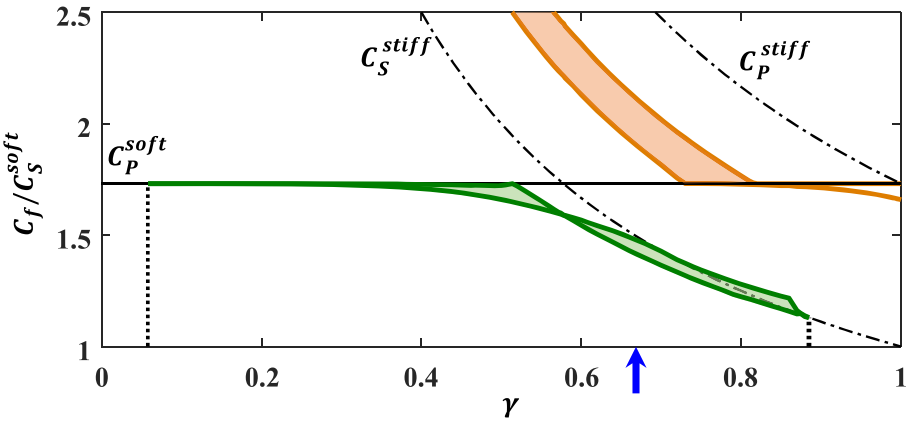

Figure 11. Phase diagram of the allowed supershear rupture velocities in the negative direction. Here, we consider a model bimaterial characterized by a single material mismatch $\gamma = C_S^{soft}/C_S^{stiff}$. The other material parameters are given by $\rho_{stiff} = \rho_{soft}$, $C_S^{stiff} = \sqrt{3}C_S^{soft}$, and $C_P^{stiff} = \sqrt{3}C_P^{soft}$. All velocities are scaled by C_S^{soft}. The dashed black curves show the variation of the different wave speeds with γ. We have two possible velocity regimes for ruptures propagating in the negative direction. The vertical dashed line corresponds to $\gamma = \gamma_c$, where the lower supershear branch disappears. Note that no upper limit for C_f exists (beyond C_P^{stiff}) as a function of γ. The ordinate axis is simply cut off at a value of 2.5. The blue arrow denotes the value of $\gamma = 0.67$, which corresponds approximately to the bimaterial contrast used in the experiments.

materials. Shaded are the evolution curves with γ of the two allowed regions (see Figure 10). An interesting prediction of the theory is the existence of critical values of $\gamma = \gamma_c$ for which the lower supershear branch disappears (while the upper branch continues for all values of γ).

5. Discussion

We have presented an in-depth study of supershear ruptures in bimaterial systems. Up to this point, nearly all of our knowledge about bimaterial supershear rupture has been numerical, and there have been very few experimental observations. We have shown that bimaterial supershear ruptures have numerous characteristic features that set them apart from ruptures along homogeneous interfaces. These characteristic features include directional prevalence, well-defined propagation velocity ranges, transition mechanisms to supershear, unique functional forms near rupture tips, and direction-dependent rupture stability. The common thread linking all of our results is that there is a clear differentiation between ruptures propagating in opposing directions. How this asymmetry results from the bimaterial coupling is explained by the theory that we present.

5.1. The Prevalence of Negatively Versus Positively Propagating Supershear Ruptures

How are bimaterial supershear ruptures excited? In homogeneous systems, it has been extensively demonstrated that it is easily possible to "overstress" a frictional system to values of applied stress that are well beyond the values needed to sustain rupture propagation (Ben-David & Fineberg, 2011; Ben-David et al., 2010; Passelègue et al., 2013). Only when the level of overstress is large have supershear ruptures been observed in these experiments. This type of behavior has also been observed in simulations of bimaterial systems (Shi & Ben-Zion, 2006). Numerical simulations have shown that heterogeneity in stress and strength, potentially linked to fault geometry (Bruhat et al., 2016; Dunham, 2007; Liu & Lapusta, 2008) or the presence of a free surface (Hu et al., 2019; Kaneko & Lapusta, 2010), can trigger supershear at low background stresses. We can't, however, yet say, a priori, which type of rupture will be selected. If a sufficient amount of energy is stored in the system, negative supershear, positive slip pulses, or positive supershear coupled to slip pulse trains (see Figure 4) may all be possible. Selection may well be dependent on the nucleation location. If, for example, ruptures are nucleated at locations away from system edges, counter-propagating ruptures (as presented in Figure 8) will be excited. If, on the other hand, a rupture nucleates near a hard barrier, then the rupture direction is determined by geometry.

Negatively propagating supershear ruptures take up 61% of all observed ruptures in the negative direction (subshear or supershear). In contrast, supershear ruptures in the positive direction are extremely rare, comprising only 2% of the total. The sparsity of supershear ruptures in the positive propagation direction is consistent with previous experimental observations (Shlomai & Fineberg, 2016; Xia et al., 2004, 2005). We would expect that observations of supershear ruptures within natural faults, which are becoming increasingly common (Bao et al., 2019; Bhat et al., 2007; Bouchon & Vallée, 2003; Dunham & Archuleta, 2004; Wang et al., 2016), should follow this pattern.

Both the predominance of the supershear ruptures relative to slower ruptures in the negative direction and the suppression of supershear ruptures in the positive direction are entirely consistent with the reversal of the sign of the bimaterial coupling observed previously (Ben-Zion, 2001; Langer et al., 2012; Ranjith & Rice, 2001; Weertman, 1980). Our self-consistent calculations significantly extend this previous work and, moreover, clearly differentiate between two distinct regimes in what is generally coined "supershear": transonic ($C_S^{soft} < C_f < C_S^{stiff}$) ruptures that exist in the positive direction and true supershear ($C_S^{soft} < C_S^{stiff} < C_f$) ruptures, which exist in the negative one. The region of existence in the positive direction has been identified (Shlomai et al., 2020) with slip pulses.

5.2. "Allowed" Velocity Ranges

Our theory predicts a general phase diagram (Figure 11) for the range of existence of supershear ruptures for any material contrast. These predictions are based on the assumption that rupture propagation cannot take place when the pressure behind the rupture tip is increased by bimaterial coupling. In the negative direction, the allowed velocity ranges (Figure 10) are thus determined dynamically via the sign of pressure variations at the interface as function of the material contrast. In this direction, the theoretical predictions of the allowed propagation velocity semiquantitatively agree with the observed range of measured supershear velocities. This mechanism is essentially independent of either the form of the friction law or the magnitude of any assumed friction coefficient. This view contrasts with predictions of Cochard and Rice (2000) and Ranjith and Rice (2001), which were dependent on the value of the friction coefficient.

The phase diagram in Figure 11 is consistent with all known measurements and numerical calculations of negative supershear velocities in bimaterial systems. These include the following:

- For the value of $\gamma \sim 0.67$ used in our experiments, all of our observed supershear velocities were above C_P^{soft} (Figure 6).
- For the value $\gamma \sim 0.8$ describing polycarbonate-homolite system (Xia et al., 2005), the observed values of supershear velocities are below C_P^{soft}.
- Predictions of Ranjith and Rice (2001) of supershear velocities slightly below C_P^{soft} for low values of γ (high velocity contrasts) that are consistent with the lower branch in Figure 11.
- Numerically observed negative supershear ruptures (Shi & Ben-Zion, 2006) that propagated slightly below C_P^{soft} for $\gamma \sim 0.8$.

Based on the increase of normal stress along the entire interface, the theory predicts that supershear ruptures shouldn't exist at all in the positive direction. Our experiments show that supershear ruptures *do* exist in the positive direction, for propagation velocities between C_S^{stiff} and C_P^{soft}. The theoretical prediction that precludes the existence of positive supershear ruptures is not, however, a "fundamental" prediction like the limiting velocity of sub-Rayleigh cracks, which is based on elastodynamics. If shear stresses, which can dynamically vary (Svetlizky et al., 2016), are sufficiently high to overcome the increased frictional resistance caused by enhanced σ_{yy}, nucleation of positive supershear ruptures could be possible, as we have seen in section 3.1. Additional mechanisms that are able to give rise to stress build-up along the interface may be roughness (our interface roughness is on the order of its 1 μm overall flatness, so local contact inhomogeneity may certainly be sufficient to form local barriers to propagation) or stress redistribution due to previous events, as observed in Ben-David et al. (2010) Bruhat et al. (2016), and Rubinstein et al. (2007).

Observed supershear velocities in the positive direction are definitely slower than supershear velocities in the negative direction. We note that the former values are significantly lower than the values approaching C_P^{stiff} that were observed numerically (Ampuero & Ben-Zion, 2008; Shi & Ben-Zion, 2006). We believe that

these differences may be due to the explicit nucleation mechanisms used in the numerical calculations, which triggered the simulated supershear ruptures at this rapid velocity.

5.3. The Transition Mechanisms to Supershear

Direct and smooth transitions from subshear to supershear are always observed in the negative direction, whereas positive direction supershear ruptures *solely* occur via a secondary (Burridge-Andrews type) transition (Figures 8 and 7). The observed transition mechanisms in both directions agree well with the numerical experiments of Langer et al. (2012).

5.4. The Functional Forms of Supershear Ruptures

The singularity of the bimaterial solution at supershear tips is weaker than the $q = 1/2$ that characterizes subshear ruptures. Beyond $C_f = C_S^{soft}$, the exponent q changes dramatically with C_f (Figure 9). This behavior is qualitatively similar to the characteristic form of supershear ruptures within homogeneous interfaces (Broberg, 1989; Svetlizky et al., 2020), although predicted values of q are, quantitatively, quite different. Dynamically reduced contact area *only* occurs at the tips of negatively propagating supershear ruptures (Figure 8). The structure of the negative supershear ruptures, while much more faint, is quite reminiscent of the slip pulse structure in the positive direction, which was shown (Shlomai & Fineberg, 2016) to clearly result from bimaterial coupling at transonic velocities.

5.5. Rupture Stability

Negative supershear ruptures (Figure 7), once excited, stably propagate. In the positive direction, where supershear ruptures are *not* predicted to exist, propagating supershear ruptures break up into trains of parallel slip pulses (Figures 4 and 5). This observation of such continuous triggering of slip pulses by supershear ruptures had not been observed previously, and such pulse trains have been rarely considered either theoretically and numerically.

We note that our theoretical analysis, paradoxically, is strictly valid only for a "frictionless" interface. The analysis explicitly does *not* take frictional coupling into account. While the theory predicts changes of σ_{yy}, one needs to tacitly assume a friction law in order to relate stress variations to frictional resistance at the interface. We believe that any friction law will yield quantitatively similar predictions for the existence of preferred propagation directions and the velocity range in which solutions exist. The explicit incorporation of nonconstant frictional resistance is an analytical as well as numerical challenge. In the transonic case, the incorporation of friction was seen to have a pronounced effect on the functional form of the solutions (friction actually gives rise to slip pulse-like localization) (Shlomai et al., 2020). These frictionless solutions are, however, important, as they are needed as a baseline for comparison.

In conclusion, our detailed measurements coupled with the elastodynamic theory derived here now provide a coherent description of the phenomenology of supershear ruptures in bimaterial systems. While some questions remain open, we believe that this work provides a firm basis for both identifying this important class of ruptures and understanding their rather unique properties.

Data Availability Statement

Supporting data for "Supershear frictional ruptures along bimaterial interfaces." 4TU Centre for Research Data. Dataset: https://doi.org/10.4121/uuid:b07d4c49-450c-461a-9367-1ee804d3c1ae.

Acknowledgments

J. F. and H. S. acknowledge the support of the Israel Science Foundation (Grant 840/19). M. A.-B. and J. F. acknowledge the support of the International Research Project "Non-Equilibrium Physics of Complex Systems" (IRP-PhyComSys, France-Israel). M. A.-B. and R. A. acknowledge the support of the Laboratoire International Associé "Matière: Structure et Dynamique" (LIA-MSD, France-Chile).

References

Albertini, G., & Kammer, D. S. (2017). Off-fault heterogeneities promote supershear transition of dynamic mode II cracks. *Journal of Geophysical Research: Solid Earth*, *122*, 6625–6641. https://doi.org/10.1002/2017JB014301

Aldam, M., Bar-Sinai, Y., Svetlizky, I., Brener, E. A., Fineberg, J., & Bouchbinder, E. (2016). Frictional sliding without geometrical reflection symmetry. *Physical Review X*, *6*(4), 41023. https://doi.org/10.1103/PhysRevX.6.041023

Aldam, M., Xu, S., Brener, E. A., Ben-Zion, Y., & Bouchbinder, E. (2017). Nonmonotonicity of the frictional bimaterial effect. *Journal of Geophysical Research: Solid Earth*, *122*, 8270–8284. https://doi.org/10.1002/2017JB014665

Ampuero, J. P., & Ben-Zion, Y. (2008). Cracks, pulses and macroscopic asymmetry of dynamic rupture on a bimaterial interface with velocity-weakening friction. *Geophysical International Journal*, *173*(2), 674–692. https://doi.org/10.1111/j.1365-246X.2008.03736.x

Andrews, D. J. (1973). A numerical study of tectonic stress release by underground explosions. *Bulletin of the Seismological Society of America*, *63*(4), 1375–1391.

Andrews, D. J. (1976). Rupture velocity of plane strain shear cracks. *Journal of Geophysical Research*, *81*, 5679.

Andrews, D. J., & Ben-Zion, Y. (1997). Wrinkle-like slip pulse on a fault between different materials. *Journal of Geophysical Research*, *102*(B1), 553–571. https://doi.org/10.1029/96JB02856

Archuleta, R. J. (1984). A faulting model for the 1979 Imperial-Valley earthquake. *Journal of Geophysical Research*, *89*(NB6), 4559–4585. https://doi.org/10.1029/JB089iB06p04559

Bao, H., Ampuero, J.-P., Meng, L., Fielding, E. J., Liang, C., Milliner, C. W. D., et al. (2019). Early and persistent supershear rupture of the 2018 magnitude 7.5 Palu earthquake. *Nature Geoscience*, *12*(3), 200–205. https://doi.org/10.1038/s41561-018-0297-z

Barras, F., Aldam, M., Roch, T., Brener, E. A., Bouchbinder, E., & Molinari, J.-F. (2020). The emergence of crack-like behavior of frictional rupture: Edge singularity and energy balance. *Earth and Planetary Science Letters*, *531*, 115978. https://doi.org/10.1016/j.epsl.2019.115978

Barras, F., Geubelle, P. H., & Molinari, J.-F. (2017). Interplay between process zone and material heterogeneities for dynamic cracks. *Physical Review Letters*, *119*(14), 144101. https://doi.org/10.1103/PhysRevLett.119.144101

Bayart, E., Svetlizky, I., & Fineberg, J. (2016a). Fracture mechanics determine the lengths of interface ruptures that mediate frictional motion. *Nature Physics*, *12*(2), 166–170.

Bayart, E., Svetlizky, I., & Fineberg, J. (2016b). Slippery but tough: The rapid fracture of lubricated frictional interfaces. *Physical Review Letters*, *116*, 194301. https://doi.org/10.1103/PhysRevLett.116.194301

Bayart, E., Svetlizky, I., & Fineberg, J. (2018). Rupture dynamics of heterogeneous frictional interfaces. *Journal of Geophysical Research: Solid Earth*, *123*, 3828–3848. https://doi.org/10.1002/2018JB015509

Ben-David, O., Cohen, G., & Fineberg, J. (2010). The dynamics of the onset of frictional slip. *Science*, *330*(6001), 211–214. https://doi.org/10.1126/science.1194777

Ben-David, O., & Fineberg, J. (2011). Static friction coefficient is not a material constant. *Physical Review Letters*, *106*, 254301. https://doi.org/10.1103/PhysRevLett.106.254301

Ben-Zion, Y. (2001). Dynamic ruptures in recent models of earthquake faults. *Journal of Mechanics and Physics of Solids*, *49*(9), 2209–2244. https://doi.org/10.1016/S0022-5096(01)00036-9

Bhat, H. S., Dmowska, R., King, G. C. P., Klinger, Y., & Rice, J. R. (2007). Off-fault damage patterns due to supershear ruptures with application to the 2001 Mw 8.1 Kokoxili (Kunlun) Tibet earthquake. *Journal of Geophysical Research*, *112*, B06301. https://doi.org/10.1029/2006JB004425

Bouchon, M., Bouin, M. P., Karabulut, H., Toksoz, M. N., Dietrich, M., & Rosakis, A. J. (2001). How fast is rupture during an earthquake? New insights from the 1999 Turkey earthquakes. *Geophysical Research Letters*, *28*(14), 2723–2726. https://doi.org/10.1029/2001GL013112

Bouchon, M., & Vallée, M. (2003). Observation of long supershear rupture during the magnitude 8.1 Kunlunshan earthquake. *Science*, *301*(5634), 824–826. https://doi.org/10.1126/science.1086832

Broberg, K. B. (1989). The near-tip field at high crack velocities. *International Journal of Fracture*, *39*(1), 1–13. https://doi.org/10.1007/BF00047435

Broberg, K. B. (1994). Intersonic bilateral slip. *Geophysical Journal International*, *119*(3), 706–714. https://doi.org/10.1111/j.1365-246X.1994.tb04010.x

Broberg, K. B. (1999). *Cracks and fracture*. San Diego: Academic Press.

Bruhat, L., Fang, Z., & Dunham, E. M. (2016). Rupture complexity and the supershear transition on rough faults. *Journal of Geophysical Research: Solid Earth*, *121*, 210–224. https://doi.org/10.1002/2015JB012512

Burridge, R. (1973). Admissible speeds for plane-strain self-similar shear cracks with friction but lacking cohesion. *Geophysical Journal of the Royal Astronomical Society*, *35*(4), 439–455.

Cochard, A., & Rice, J. R. (2000). Fault rupture between dissimilar materials: Ill-posedness, regularization, and slip-pulse response. *Journal of Geophysical Research*, *105*(B11), 25,891–25,907. https://doi.org/10.1029/2000JB900230

Dor, O., Ben-Zion, Y., Rockwell, T. K., & Brune, J. (2006). Pulverized rocks in the Mojave section of the San Andreas fault zone. *Earth and Planetary Science Letters*, *245*(3–4), 642–654. https://doi.org/10.1016/j.epsl.2006.03.034

Dor, O., Yildirim, C., Rockwell, T. K., Ben-Zion, Y., Emre, O., Sisk, M., & Duman, T. Y. (2008). Geological and geomorphologic asymmetry across the rupture zones of the 1943 and 1944 earthquakes on the North Anatolian Fault: Possible signals for preferred earthquake propagation direction. *Geophysical Journal International*, *173*(2), 483–504. https://doi.org/10.1111/j.1365-246X.2008.03709.x

Dunham, E. M. (2007). Conditions governing the occurrence of supershear ruptures under slip-weakening friction. *Journal of Geophysical Research*, *112*, B07302. https://doi.org/10.1029/2006JB004717

Dunham, E. M., & Archuleta, R. J. (2004). Evidence for a supershear transient during the 2002 Denali fault earthquake. *Bulletin of the Seismological Society of America*, *94*(6B), S256. https://doi.org/10.1785/0120040616

Dunham, E. M., Favreau, P., & Carlson, J. M. (2003). A supershear transition mechanism for cracks. *Science*, *299*(5612), 1557–1559. https://doi.org/10.1126/science.1080650

Freund, L. B. (1990). *Dynamic fracture mechanics*. New York: Cambridge University Press.

Harris, R. A., & Day, S. M. (1997). Effects of a low-velocity zone on a dynamic rupture. *Bulletin of the Seismological Society of America*, *87*, 1267–1280.

Hu, F., Oglesby, D. D., & Chen, X. (2019). The sustainability of free-surface-induced supershear rupture on strike-slip faults. *Geophysical Research Letters*, *46*, 9537–9543. https://doi.org/10.1029/2019GL084318

Kammer, D. S., Svetlizky, I., Cohen, G., & Fineberg, J. (2018). The equation of motion for supershear frictional rupture fronts. *Science Advances*, *4*(7), eaat5622. https://doi.org/10.1126/sciadv.aat5622

Kaneko, Y., & Lapusta, N. (2010). Supershear transition due to a free surface in 3-D simulations of spontaneous dynamic rupture on vertical strike-slip faults. *Tectonophysics*, *493*(3-4, SI), 272–284. https://doi.org/10.1016/j.tecto.2010.06.015

Lambros, S. J., & Rosakis, A. J. (1995a). Dynamic decohesion of bimaterial—Experimental-observations and failure criteria. *International Journal of Solids and Structures*, *32*(17-18), 2677–2702. International Symposium on Dynamic Failure Mechanics of Modern Materials, Calif Inst Technol, Pasadena, CA, 1994.

Lambros, S. J., & Rosakis, A. J. (1995b). Shear dominated transonic interfacial crack-growth in a bimaterial. 1. Experimental-observations. *Journal of the Mechanics and Physics of Solids*, *43*(2), 169–188. https://doi.org/10.1016/0022-5096(94)00071-C

Langer, S., Olsen-Kettle, L., & Weatherley, D. (2012). Identification of supershear transition mechanisms due to material contrast at bimaterial faults. *Geophysical Journal International*, *190*(2), 1169–1180. https://doi.org/10.1111/j.1365-246X.2012.05535.x

Lei, J., & Zhao, D. (2009). Structural heterogeneity of the Longmenshan fault zone and the mechanism of the 2008 Wenchuan earthquake (Ms 8.0). *Geochemistry Geophysics Geosystems*, *10*, Q10010. https://doi.org/10.1029/2009GC002590

Liu, C., Bizzarri, A., & Das, S. (2014). Progression of spontaneous in-plane shear faults from sub-Rayleigh to compressional wave rupture speeds. *Journal of Geophysical Research: Solid Earth*, *119*, 8331–8345. https://doi.org/10.1002/2014JB011187

Liu, C., Huang, Y., & Rosakis, A. J. (1995). Shear dominated transonic interfacial crack-growth in a bimaterial. 2. Asymptotic fields and favorable velocity regimes. *Journal of the Mechanics and Physics of Solids*, *43*(2), 189–206. https://doi.org/10.1016/0022-5096(94)00072-D

Liu, Y., & Lapusta, N. (2008). Transition of mode II cracks from sub-Rayleigh to intersonic speeds in the presence of favorable heterogeneity. *Journal of the Mechanics and Physics of Solids*, *56*, 25–50.

Ma, S., & Beroza, G. C. (2008). Rupture dynamics on a bimaterial interface for dipping faults. *Bulletin of the Seismological Society of America*, *98*(4), 1642–1658. https://doi.org/10.1785/0120070201

McGuire, J., & Ben-Zion, Y. (2005). High-resolution imaging of the Bear Valley section of the San Andreas fault at seismogenic depths with fault-zone head waves and relocated seismicity. *Geophysical Journal International*, *163*(1), 152–164. https://doi.org/10.1111/j.1365-246X.2005.02703.x

Mello, M., Bhat, H. S., & Rosakis, A. J. (2016). Spatiotemporal properties of sub-Rayleigh and supershear rupture velocity fields: Theory and experiments. *Journal of the Mechanics and Physics of Solids*, *93*, 153–181. https://doi.org/10.1016/j.jmps.2016.02.031

Mello, M., Bhat, H. S., Rosakis, A. J., & Kanamori, H. (2010). Identifying the unique ground motion signatures of supershear earthquakes: Theory and experiments. *Tectonophysics*, *493*(3), 297–326. Earthquake supershear rupture speeds.

Passelègue, F. X., Schubnel, A., Nielsen, S., Bhat, H. S., & Madariaga, R. (2013). From sub-Rayleigh to supershear ruptures during stick-slip experiments on crustal rocks. *Science*, *340*(6137), 1208–1211. https://doi.org/10.1126/science.1235637

Ranjith, K., & Rice, J. R. (2001). Slip dynamics at an interface between dissimilar materials. *Journal of Mechanics and Physics of Solids*, *49*(2), 341–361. https://doi.org/10.1016/S0022-5096(00)00029-6

Read, B. E., & Duncan, J. C. (1981). Measurement of dynamic properties of polymeric glasses for different modes of deformation. *Polymer Testing*, *2*(2), 135–150. https://doi.org/10.1016/0142-9418(81)90031-3

Rice, J. R., Lapusta, N., & Ranjith, K. (2001). Rate and state dependent friction and the stability of sliding between elastically deformable solids. *Journal of the Mechanics and Physics of Solids*, *49*(9), 1865–1898. https://doi.org/10.1016/S0022-5096(01)00042-4

Rosakis, A. J., Samudrala, O., & Coker, D. (1999). Cracks faster than the shear wave speed. *Science*, *284*(5418), 1337–1340. https://doi.org/10.1126/science.284.5418.1337

Rosakis, A. J., Xia, K., Lykotrafitis, G., & Kanamori, H. (2007). 4.08—Dynamic shear rupture in frictional interfaces: Speeds, directionality, and modes, (Second Edition). In G. Schubert (Ed.), *Treatise on geophysics* (pp. 183–213). Oxford: Elsevier. https://doi.org/10.1016/B978-0-444-53802-4.00072-5

Rubin, A. M., & Ampuero, J.-P. (2007). Aftershock asymmetry on a bimaterial interface. *Journal of Geophysical Research*, *112*, B05307. https://doi.org/10.1029/2006JB004337

Rubinstein, S. M., Cohen, G., & Fineberg, J. (2004). Detachment fronts and the onset of dynamic friction. *Nature*, *430*(7003), 1005–1009.

Rubinstein, S. M., Cohen, G., & Fineberg, J. (2007). Dynamics of precursors to frictional sliding. *Physical Review Letters*, *98*(22), 226,103.

Rubinstein, S. M., Cohen, G., & Fineberg, J. (2009). Visualizing stick slip: Experimental observations of processes governing the nucleation of frictional sliding. *Journal of Physics D: Applied Physics*, *42*(21), 214,016.

Rubinstein, S. M., Shay, M., Cohen, G., & Fineberg, J. (2006). Crack-like processes governing the onset of frictional slip. *International Journal of Fracture*, *140*(1), 201–212. https://doi.org/10.1007/s10704-006-0049-8

Scala, A., Festa, G., & Vilotte, J.-P. (2017). Rupture dynamics along bimaterial interfaces: A parametric study of the shear-normal traction coupling. *Geophysical Journal International*, *209*(1), 48–67. https://doi.org/10.1093/gji/ggw489

Scholz, C. H. (2002). *The mechanics of earthquakes and faulting* (2nd ed.). Cambridge: Cambridge University Press.

Shi, Z., & Ben-Zion, Y. (2006). Dynamic rupture on a bimaterial interface governed by slip-weakening friction. *Geophysical Journal International*, *165*, 469–484.

Shlomai, H., & Fineberg, J. (2016). The structure of slip-pulses and supershear ruptures driving slip in bimaterial friction. *Nature Communications*, *7*, 11,787. https://doi.org/10.1038/ncomms11787

Shlomai, H., Kammer, D. S., Adda-Bedia, M., & Fineberg, J. (2020). The onset of the frictional motion of dissimilar materials. *Proceedings of the National Academy of Sciences*, *117*, 13,379–13,385. https://doi.org/10.1073/pnas.1916869117

Svetlizky, I., Albertini, G., Cohen, G., Kammer, D. S., & Fineberg, J. (2020). Dynamic fields at the tip of sub-Rayleigh and supershear frictional rupture fronts. *Journal of the Mechanics and Physics of Solids*, *137*, 103826. https://doi.org/10.1016/jmps.2019.103826

Svetlizky, I., Bayart, E., Cohen, G., & Fineberg, J. (2017). Frictional resistance within the wake of frictional rupture fronts. *Physical Review Letters*, *118*, 234,301. https://doi.org/10.1103/PhysRevLett.118.234301

Svetlizky, I., & Fineberg, J. (2014). Classical shear cracks drive the onset of dry frictional motion. *Nature*, *509*(7499), 205–208.

Svetlizky, I., Kammer, D. S., Bayart, E., Cohen, G., & Fineberg, J. (2017). Brittle fracture theory predicts the equation of motion of frictional rupture fronts. *Physical Review Letters*, *118*, 125501. https://doi.org/10.1103/PhysRevLett.118.125501

Svetlizky, I., Pino Muñoz, D., Radiguet, M., Kammer, D. S., Molinari, J.-F., & Fineberg, J. (2016). Properties of the shear stress peak radiated ahead of rapidly accelerating rupture fronts that mediate frictional slip. *Proceedings of the National Academy of Sciences*, *113*(3), 542–547. https://doi.org/10.1073/pnas.1517545113

Wang, W., Huang, Y., Rosakis, A. J., & Liu, C. (1998). Effect of elastic mismatch in intersonic crack propagation along a bimaterial interface. *Engineering Fracture Mechanics*, *61*(5-6), 471–485. https://doi.org/10.1016/S0013-7944(98)00089-7

Wang, D., Mori, J., & Koketsu, K. (2016). Fast rupture propagation for large strike-slip earthquakes. *Earth and Planetary Science Letters*, *440*, 115–126. https://doi.org/10.1016/j.epsl.2016.02.022

Weertman, J. J. (1980). Unstable slippage across a fault that separates elastic media of different elastic constants. *Journal of Geophysical Research*, *85*, 1455–1461.

Xia, K. W., Rosakis, A. J., & Kanamori, H. (2004). Laboratory earthquakes: The sub-Rayleigh-to-supershear rupture transition. *Science*, *303*(5665), 1859–1861. https://doi.org/10.1126/science.1094022

Xia, K. W., Rosakis, A. J., Kanamori, H., & Rice, J. R. (2005). Laboratory earthquakes along inhomogeneous faults: Directionality and supershear. *Science*, *308*(5722), 681–684. https://doi.org/10.1126/science.1108193